Surface & Coatings Technology 458 (2023) 129363

Contents lists available at ScienceDirect

Surface & Coatings Technology

journal homepage: www.elsevier.com/locate/surfcoat

Texturization of polycrystalline titanium surfaces after low-energy ion-beam irradiation: Impact on biocompatibility

M.A. Garcia [a,d,*], R. Gago [b], M. Arroyo-Hernández [c], E.H. de Laorden [c], M. Iglesias [c], D. Esteban-Mendoza [b], R. Cuerno [e], J. Rickards [d]

[a] Facultad de Ciencias, and Posgrado en Ciencias Físicas, Universidad Nacional Autónoma de México (UNAM), Apartado Postal 20-364, 01000 Ciudad de México, Mexico
[b] Instituto de Ciencia de Materiales de Madrid, Consejo Superior de Investigaciones Científicas (CSIC), 28049 Madrid, Spain
[c] Facultad de Ciencias Experimentales, Universidad Francisco de Vitoria, 28223 Pozuelo de Alarcón, Spain
[d] Instituto de Física, Universidad Nacional Autónoma de México (UNAM), Apartado Postal 20-364, 01000 Ciudad de México, Mexico
[e] Departamento de Matemáticas and Grupo Interdisciplinar de Sistemas Complejos (GISC), Universidad Carlos III de Madrid, 28911 Leganés, Spain

ARTICLE INFO

Keywords:
Titanium
Ion irradiation
Pattern formation
Wetting
Biological assays

ABSTRACT

In this study, the impact of low-energy (1 keV) Ar^+ ion-beam irradiation on the morphology of polycrystalline Ti disks was investigated. Targets were prepared by cutting and mechanically polishing commercial rods. The surface topographies before and after irradiation were characterized by scanning electron microscopy (SEM) and mechanical profilometry. Irradiation was performed using a wide range of incident angles (α_i) from normal to grazing geometries at a total dose of 10^{18} ions/cm^2. SEM analysis of the irradiated Ti targets revealed clear texturing with various attainable surface morphologies depending on α_i. The surface features varied from ripples within patches with fingerprint-like patterns ($0 \leq \alpha_i \leq 60^\circ$) to oriented structures parallel to the direction of the ion beam, such as pillar/tip structures ($65 \leq \alpha_i \leq 75^\circ$) and shallow ripples ($\alpha_i \approx 80^\circ$). This morphological selectivity could be attributed to the competitive diffusive and erosive regimes, where the lateral uniformity of the morphology was affected by the limited size of the crystal grains. Finally, the wettability and biocompatibility of the characteristic topographies were evaluated, and the results indicated improved performance of the ion-beam-textured surfaces compared to the untreated ones.

1. Introduction

The surface modification of Ti-based materials is an active research area for their application in biomedical implants. Metallic biomaterials, including Ti and its alloys, can be potentially used in orthopedic implants (e.g., for total hip replacement) and dental implants owing to their intrinsic physical properties with respect to the hard tissue [1–3]. The biocompatibility, high strength, low weight, and corrosion resistance are the key physical properties of Ti-based materials that have enabled their use in the biomedical field. However, their complete surface compliance with the human body has not yet been achieved. This is possibly because of the lack of control over bio-chemical processes at the metal–bone interface [4]. That is, the metallic biomaterial and the hard tissue require similar physical properties. This is often achieved by considering both the tensile strength and the elastic modulus of the metal implant. In such instances, distinct properties on the bulk properties give rise to the stress-shielding effect [5,6]. Under this situation, the stress-shielding effect leads to atrophy of the hard tissue at the surrounding metal implant, consequently degrading the adhering capacity at the bone-metal interface. For this reason, the overall performance of the implant diminishes such that it can lead to the ultimate failure of a biomedical implant, necessitating further surgical intervention. The aforementioned challenges have hindered the long-term usage of biocompatible alloys for hard tissue replacement (e.g., orthopedic implants).

Although, surface modification techniques cannot address the bulk physical properties mismatch, it can enable functionalization at the nano and micro scales [7–9]. Through surface modification, specific surface topographies can be obtained using diverse methods such as ion irradiation [10,11] and laser treatments [12,13]. The local and global

* Corresponding author at: Facultad de Ciencias, and Posgrado en Ciencias Físicas, Universidad Nacional Autónoma de México (UNAM), Apartado Postal 20-364, 01000 Ciudad de México, Mexico.
E-mail address: magarcia@ciencias.unam.mx (M.A. Garcia).

https://doi.org/10.1016/j.surfcoat.2023.129363
Received 25 June 2022; Received in revised form 10 February 2023; Accepted 15 February 2023
Available online 20 February 2023

roughness of these surfaces may enhance the bio-chemical and physical surface properties at the interface. In the case of polycrystalline materials, local roughness corresponds to those characterized by individual grains, meanwhile global roughness overlaps many grains, respectively. Moreover, surface roughness links the surface topography to its surface energy. Surfaces in contact with fluids are quantified by the static contact angle measurement [2]. Thus, surface energetics at the surface play important roles in the interaction with its environment. A previous study [4] showed that a variation in the length scales of surface topographies may improve bio-chemical processes such that the modified surfaces can act as a linkage for metals to contact soft or hard tissue. These length scales can extend to the nanometer range, where nanostructuring can also have a considerable impact on biomedical applications [14]. The broad range of available scales upon surface texturing can also contribute to other possible applications apart from biomedical implants, such as medical instrumentation and devices [15]. Hence, control over small length scales, such as those used for analytical systems, would permit the combination of drugs and devices to characterize and/or deliver biofluids in biological systems [8]. While synthesized nanostructures have found new applications, subsequent surface treatments [16] may be necessary to meet biomedical requirements for use in the targeted final products.

Ion-beam irradiation is a well-established method to tailor the surface morphology of solid targets. There is particular research interest in understanding the conditions that drive the intriguing emergence of self-organized patterns [17]. A study found that surface structures like ripples or mounds can be produced at the nanoscale using ion-beam irradiation, akin to those macroscopically observed in sand dunes [18]. Therefore, the process is also referred as ion sand blasting [19]. Nanopatterns are generated by ion irradiation in solid targets including semiconductors [20], metals [21,22], and insulators [23–25]. The final features can be tailored using the relationship between the experimental conditions (such as ion type and energy, and incidence angle) and the physical properties of the target material. The pattern characteristics depend on the different physical mechanisms that occur due to the ion-solid interaction, such as sputtering, mass transport, surface diffusion, or defect formation [17,20]. Metal surfaces represent a special case within the field of ion-beam surface nanostructuring [19]. With metal surfaces, the high efficiency of surface-diffusion processes and the existence of diffusion restrictions such as Ehrlich–Schwoebel (ES) surface barriers typically dictate the pattern characteristics based on geometrical considerations imposed by the ion-beam direction [21,22]. Further, in polycrystalline targets, the finite size of the crystal grains and their texture (crystalline orientation) with respect to the target surface also affect the pattern characteristics and overall uniformity of the surface morphology [26,27].

The generation of surface nanopatterns by ion beams has been recently reviewed in the field of bio-applications [28,29]. As expected, the reviews discussed studies on the irradiation of Ti-based biomedical surfaces. For example, ion-beam etching and its impact on cell adhesion were reported for Ti-6Al-4V alloys [31,32]. The generation of ion-beam nanopatterns on pure Ti surfaces was also reported recently for low ion energies (<2 keV) [32,33]. Ti-6Al-4V and Ti targets have also been beam-irradiated at a high ion energy (1 MeV) with Au^+ [34], inducing the formation of large surface structures. In this context, the use of alloys has a potential of obtaining different morphologies based upon composition. Hence, the purpose of the present work is to study the low-energy ion-beam texturing of Ti targets using a wide range of incident angles. In comparison with Ti alloys, pure Ti is a simpler system, for which the eventual effects on the morphological evolution arising from compositional issues can be discarded [35]. Finally, the surface energetics and biological assays are studied to determine the bioactivity of the treated substrates.

2. Materials and methods

Commercially pure (99.6+ %) polycrystalline Ti (cpTi, grade 4) rods of diameter 1 cm were purchased from Goodfellow Corp. [36]. The rods were cut into small disks (~3 mm thickness) and polished mechanically to a mirror-like finish. Polishing was performed in successive stages using silicon carbide (SiC) grinding papers with different Federation of European Producers of Abrasives (FEPA) gradings (P360, P400, P600, P1200, and P4000), alumina powder (300 nm, α-Al_2O_3), and finally, using a 20 nm colloidal silica suspension. After polishing, the targets were clean ultrasonically in ethyl alcohol and air-dried.

Surface modification of the Ti targets was performed through low-energy (≤1 keV) noble ion-beam irradiation using a Kaufman-type ion source with a 3 cm beam diameter. The ion source was located 15 cm away from the targets. The beam profile presents a Gaussian-type curve along the radial axis with a width that increases due to the beam divergence from the source. The full width at half maximum (FWHM) of the beam profile at the working distance is about 6 cm, as extracted by the measurements with a movable Faraday Cup attached to the sample holder. In this configuration the ion beam current is homogenous over an area of 2 × 2 cm^2 within 1 % deviation. Ion-beam irradiation was performed using 1 keV Ar^+. The base pressure in the experimental vacuum chamber was around 10^{-6} mbar, while the Ar working pressure was 2 × 10^{-4} mbar. The ion current density was ~500 μA/cm^2, which was measured before the irradiation with a Faraday cup located in a movable shutter in front of the sample holder. As the sample holder was not water cooled, this ion current density led to a maximum increase of the holder temperature of ~100 °C. Meanwhile, impact of target temperatures on the resulting surface morphologies has only been attained for values higher than 400 °C. The angle of ion incidence (α_i) with respect to the surface normal was varied between 0° and 80°, and the irradiation was performed for a total dose of 10^{18} ions cm^{-2}. The established ion dose is above the threshold for morphological features to appear with a well-defined pattern type. Also, this removes surface irregularities induced by the polishing procedure (such as scratches, impurities, etc.). For such condition, experiments last from few minutes up to half an hour from normal to near grazing-incidence angles, respectively.

After ion irradiation, the surface morphology of the substrates was examined through field-emission scanning electron microscopy (FE-SEM) with FEI Verios 460 and FEI Nova NanoSEM230 (Thermo-Fisher Scientific Ltd.) microscopes. For quantification, the surface topography was characterized by mechanical profilometry (Dektak 150, Veeco Instruments Inc.). The measured quantity for the roughness analysis was Ra (average roughness) as obtained from the stylus profiler Dektak 150 software. At least five profiles measurement were carried out for each experimental condition. Wettability measurements were performed with ultra-pure (Milli-Q) water using a static contact angle instrument (CAM 101, KSV Instrument Ltd.). MilliQ droplets were deposited on irradiated surfaces, and its static contact angle was measured. The results were averaged over at least four measurements per sample at different surface locations.

Biological assays were carried out on the irradiated surfaces to test their biocompatibility. The cell proliferation was measured by the reduction of 3-[4,5-dimethylthiazol-2-yl]-2,5-diphenyltetrazolium bromide (MTT) by mitochondrial enzymes following the manufacturer's instructions (Calbiochem). The MTT assays produced formazan, which is purple in color and can be detected by absorbance measurements [37]. The tests were performed by seeding the surfaces with human placenta mesenchymal stem cells (hPMSCs; Cellular Engineering Technologies, Coralville, EE.UU., CET Catalog # HMSC.AM-100) at a density of 10^4 cells/cm^2. The cell culture was supplemented with 10 % fetal bovine serum (FBS; Lonza), Pen/Strep/Fung 10k/10k/25 mg 100× (Lonza), L-glutamine 200 mM 100× (Lonza), and hFGF-basic (10 ng/mL final; Invitrogen). The cell culture was left for 72 or 144 h under an ambient condition of 37 °C with 5 % CO_2 in Dulbecco's Modified Eagle's Medium

(DMEM) with 4.51 g/L glucose. Cells of the same density were seeded directly on the multiwell cell-culture plate (Corning Falcon P48) as a positive control in the evaluation of the viability and proliferation of the cells. Two measurements for each condition were performed.

3. Results and discussion

3.1. Surface morphology

The irradiated Ti targets present a variation in the surface morphology that strongly depends on α_i, as shown in Fig. 1. The

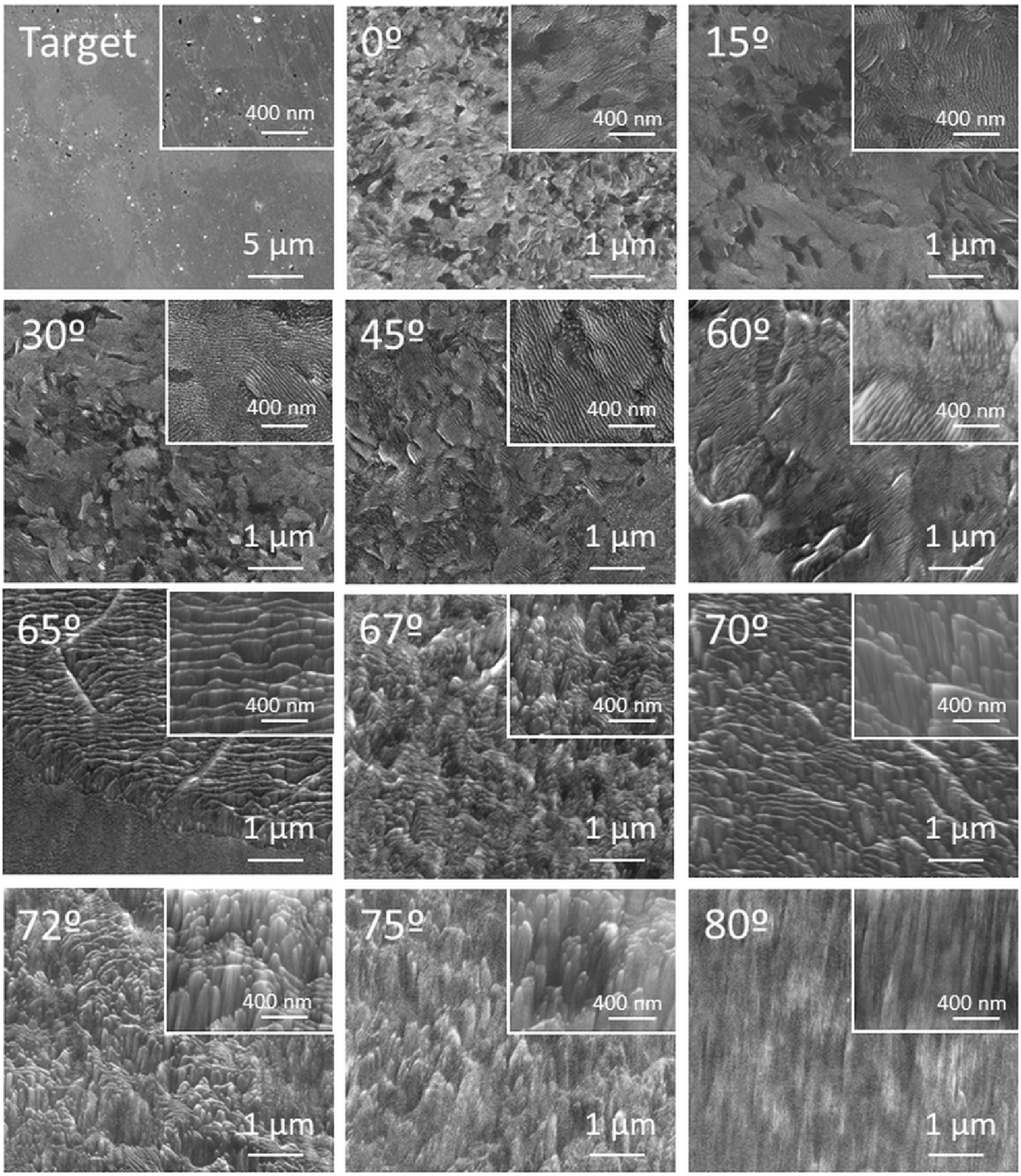

Fig. 1. FE-SEM images of pristine Ti surfaces and Ti surfaces irradiated with 1 keV Ar^+ at different α_i values for a dose of 10^{18} ions/cm^2. The projection of the ion beam direction on the surface runs from top to bottom in all micrographs of the irradiated samples.

projection of the ion beam direction onto the surface runs from top to bottom on all the FE-SEM images. The figure also shows micrographs exhibiting the typical surface of the pristine target after mechanical polishing, as an indication of the initial target state. This surface is rather featureless, except for some scratches and small residuals from the polishing material. Moreover, the (local) surface roughness of the targets after polishing is below ~2 nm, as measured by atomic force microscopy. The initial state and polycrystalline nature of the targets imply that texturing has some limitations in inducing lateral uniformity. Hence, there should be focus on the remains from the grinding material after polishing, which can considerably affect the morphological features induced by the ion-beam irradiation.

From the images in Fig. 1, three main morphological regimes are identified in the irradiated surfaces as a function of α_i. First, patches of ripples arranged into fingerprint-like patterns are generated at near-normal incidence ($\alpha_i = 0°$) and $\alpha_i \approx 60°$. These regions consist of curved parallel grooves that extend over areas ranging from a few hundreds of nanometers up to few micrometers. Notably, inside each patch, the ripples present a high degree of ordering, as evidenced by the high-magnification images shown in the insets. However, there appears to be a lack of coherence between the different domains, which can be attributed to the polycrystalline nature of the targets whereby the grain boundaries and crystalline orientations can tune the direction, length, and number of grooves. Thus, ion irradiation of polycrystalline substrates is limited by the grain boundaries, where randomly oriented crystals progressively emerged. This situation implies a lateral inhomogeneity in the resulting morphologies throughout the target surface. On the other hand, the identification of the orientation of each individual grain size is not accessible, as well as the location of the grain boundaries. For the latter reason, high temperature experiments have been also performed to reveal the grain size distribution and its eventual correlation with the pattern variation. Similar ripples on Ti surfaces produced under normal ion incidence have also been reported by Bauer et al. [32], where the characteristic wavelength was suggested to be correlated with the local crystallographic orientation with respect to the ion beam. For $\alpha_i \geq 65°$, the morphology exhibits faceting, with the formation of terraces perpendicular to the direction of the ion beam. This formation could suggest the occurrence of shadowing effects [38] during the topographical evolution, as already observed in the nanostructuring of polycrystalline metal films [27,39,40]. Such terraces are confined to regions of several microns, and coexist with regions covered with tip structures. The latter morphologies are observed in the lower part of the FE-SEM image in Fig. 1. The tips are more evident at larger angles, as seen in the high-magnification micrographs at $\alpha_i > 70°$. These structures display a pillar- or needle-like shape, with the latter being more evident in the micrograph of the sample at $\alpha_i = 75°$. Such morphologies are directed toward the incoming ion beam. Similar tip structures were reported in Ti-6Al-4V targets by Riedel et al. [30], which were generated with 700 eV Ar^+ at an angle of 75°. Such elongated structures could arise from the inhomogeneous erosion of the terraces, as discussed subsequently. Finally, at grazing incidence ($\alpha_i \approx 80°$), the surface morphology appears to be smoother and more homogeneous. In this case, shallow ripples with ridges parallel to the ion-beam direction can be observed. Note that similarly oriented ripples have been reported [27,40] for several metal surfaces under grazing-incidence irradiation.

Due to the lateral inhomogeneity of the polycrystalline samples, a quantitative analysis of the large-scale surface average roughness (Ra) was carried out using a mechanical surface profiler since it allows for surface scans in the millimeter range. The obtained values are plotted in Fig. 2(a), where the different morphological regions are highlighted by a background color. The large-scale average roughness of the pristine targets is approximately 30 ± 10 nm. In agreement with the morphologies displayed in Fig. 1, the roughness remains nearly constant from normal to oblique incidence up to $\alpha_i \approx 60°$. In this case, the roughness (~25 nm) is slightly below that of the pristine targets, indicating that the ion-beam-induced texturization in this range primarily affects the local

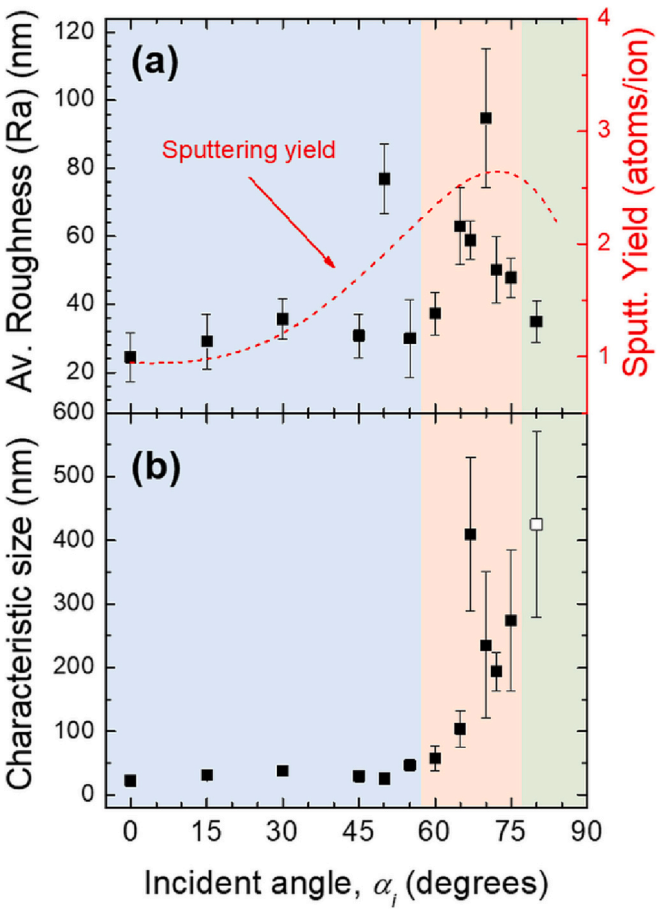

Fig. 2. (a) Long-range surface average roughness (Ra) after irradiation at different α_i values, obtained by profilometry. The sputtering yield dependence with the angle of incidence has been drawn as guide. (b) Characteristic lateral length of the surface structures at different α_i values, extracted from the analysis of the FE-SEM images.

roughness. The morphological change for $\alpha_i \geq 65°$ causes an increase in the global roughness, which reaches a maximum of ~90 nm at $\alpha_i = 70°$. Finally, the surface smoothens out for grazing incidence ($\alpha_i \approx 80°$), with the roughness again reverting to ~30 nm. Note that the change trend of the roughness with α_i approximately follows the dependence of the sputtering yield (red curve), as extracted from the SRIM code [41]. This trend has also been reported in semiconductor materials [42], indicating that the roughening is partially related to the surface erosion rate. Here, the etched depth is estimated as ~150 nm at normal incidence and can increase up to nearly ~500 nm for the highest rate at an α_i of 75°.

The characteristic size of the surface features was also determined from the FE-SEM images using Gwyddion software [43] and is displayed in Fig. 2(b). The size of the ripples produced for $\alpha_i \leq 60°$ appears to be nearly constant, with a typical wavelength of ~30 nm. On the other hand, there is a pronounced increase in the feature amplitude for $\alpha_i \geq 65°$, corresponding to the formation of facets and tips. The base of such tips or needles measures between 50 and 200 nm, and their length can reach 400 nm. The characteristic lateral size at $\alpha_i = 80°$ for the shallow ripple morphology (open square) further increases. Note that, in this case, the characteristic length corresponds to distances parallel to the ion-beam projection.

The observed morphology in our irradiated targets can be interpreted in terms of the surface-diffusion and ion-erosion mechanisms, as is frequently the case in the ion-induced nanostructuring of metal surfaces [19]. In particular, the dominance of surface-diffusion mechanisms can be attributed to the morphologies produced at $\alpha_i \leq 60°$, whereas that of ion-erosion mechanisms occurs at $60° < \alpha_i \leq 65°$ due to the enhanced

sputtering yield at large incident angles. The process window where surface diffusion dominates is further confirmed by the formation of similar patterns in a wide range of incident angles ($\alpha_i \leq 60°$) and by the lack of geometrical correlations between the features obtained and the ion-beam direction. In contrast, the ion beam seems to define (sculpt) the features for $60° < \alpha_i \leq 65°$. This interpretation can be further supported by equivalent experiments performed under axial rotation of the target during irradiation. Fig. 3 shows the FE-SEM images of the Ti targets irradiated under simultaneous rotation at 5 rpm for selected α_i values. The morphologies display random patches of ripples and, hence, retain a certain degree of similarity with respect to the static configuration (Fig. 1) for α_i values of 0° and 45°. The reminiscence of these patterns imply that the morphologies are not controlled by the ion beam, as expected in the diffusive regime of ion-beam irradiation [19–22]. However, such patches seem to be smaller than in the case of static targets. On the contrary, for $\alpha_i = 75°$, the surface seems to be smoother and the oriented features vanish, leading to an isotropic and homogenous cellular-like morphology. A similar result is obtained at $\alpha_i = 80°$, indicating that the shallow ripples also have an erosive origin. This trend is strongly reminiscent of that recently obtained experimentally in the low-energy ion-beam irradiation of rotated highly oriented pyrolytic graphite, where the initial grain structure induces coarsening of an isotropic cellular structure at sufficiently large time and length scales [26]. In general, semiconductor, insulator, and metallic targets are expected to behave most similarly under irradiation precisely in the erosive regime [19,22], as the conditions are such that the crystalline structure has no effect on the primary properties of the formed surface nanopattern, like the structure orientation and shape.

Another aspect to be analyzed after ion-beam-induced texturization is the lateral homogeneity of the topographical features. Fig. 4 shows low-magnification broad views of the irradiated samples at different α_i values (note the different scales in the images shown in Figs. 3 and 4). The surface irradiated at near-normal incidence ($\alpha_i = 15°$) is smooth at this scale, and traces of polishing scratches are still evident (in this case, the estimated etched thickness is ~150 nm). The long-range morphology is still homogeneous for the sample irradiated at $\alpha_i = 60°$, but the ion-induced fine structure is more pronounced. There is a significant change in the morphology above this angle, as illustrated in the topography of the sample irradiated at $\alpha_i = 70°$. In this case, regions sized several micrometers are observed, which are decorated with morphological features such as terraces or tips, akin to those described in Fig. 1. The contrast between these regions may be related to the type of structures, but the FE-SEM images also suggest different heights (and angles). The latter would imply that the etching rates are different between these regions. Interestingly, Bauer et al. [32] also reported a correlation between the induced morphology and local etching rate of Ti surfaces for each crystallite due to their orientation with the surface normal. Finally, at grazing incidence ($\alpha_i = 80°$), the surface morphology is rather homogeneous, which can be associated with the relatively high erosion rate and shallow penetration of ions.

To obtain information about the Ti microstructure, we performed irradiation at different target temperatures. We found that irradiation at temperatures above 500 °C can expose the grain structure. This is confirmed by the images in the bottom row of Fig. 4 for irradiation at 600 °C and $\alpha_i = 60°$ and 75°. The images show grains that correlate with the observed regions for the sample irradiated at room temperature and $\alpha_i = 70°$. Note that under irradiation at a high temperature, homogeneous ripple structures are generated within such grains with clear interfaces (barriers) defined by the grain boundaries. The structuring within the grains seems to be enhanced at a larger α_i, as expected due to the increased sputtering. Further, the wavelength of these structures is relatively large (ranging from hundreds of nanometers to micrometers) in comparison with the structures obtained at room temperature. These results can be understood in terms of the promotion of surface-diffusion

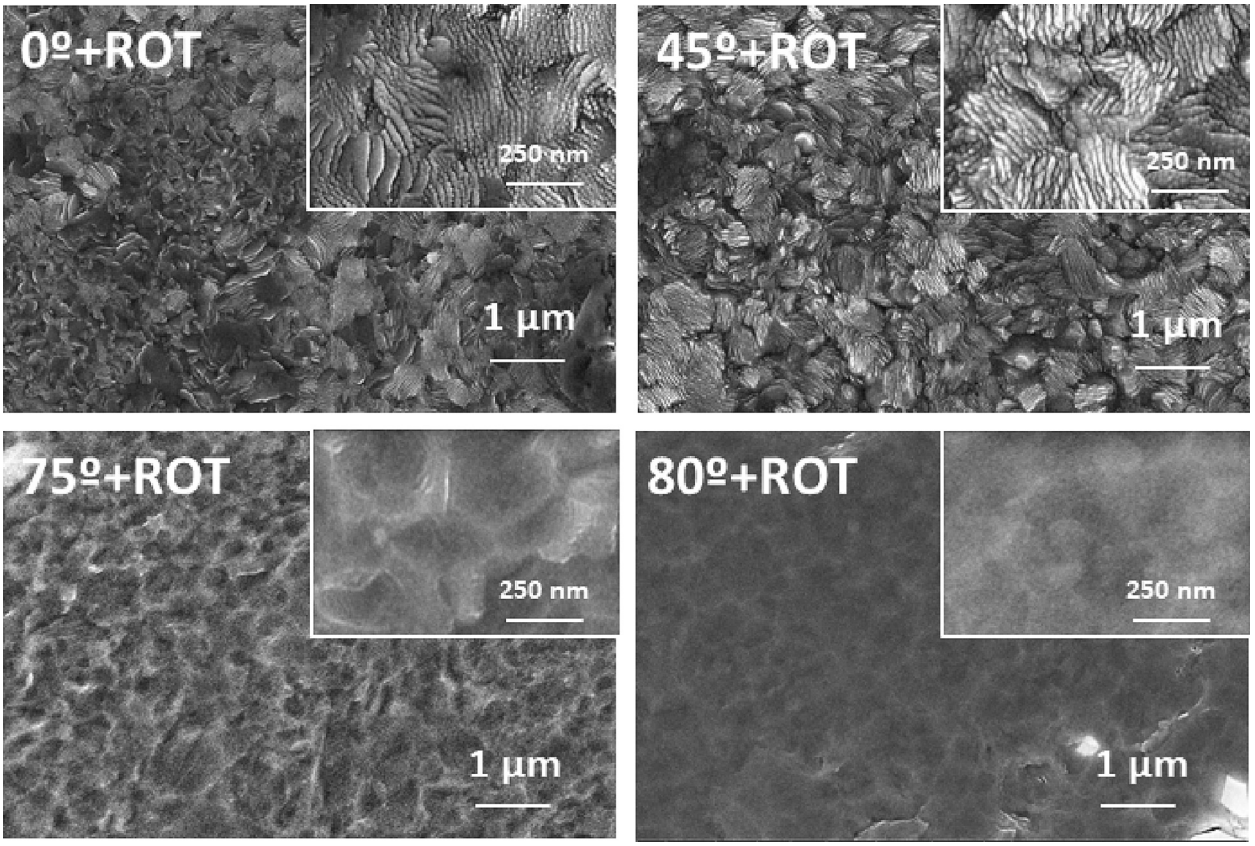

Fig. 3. FE-SEM images of Ti targets irradiated with 1 keV Ar^+ under different α_i values and simultaneously axially rotated (5 rpm) for a dose of 10^{18} ions/cm^2.

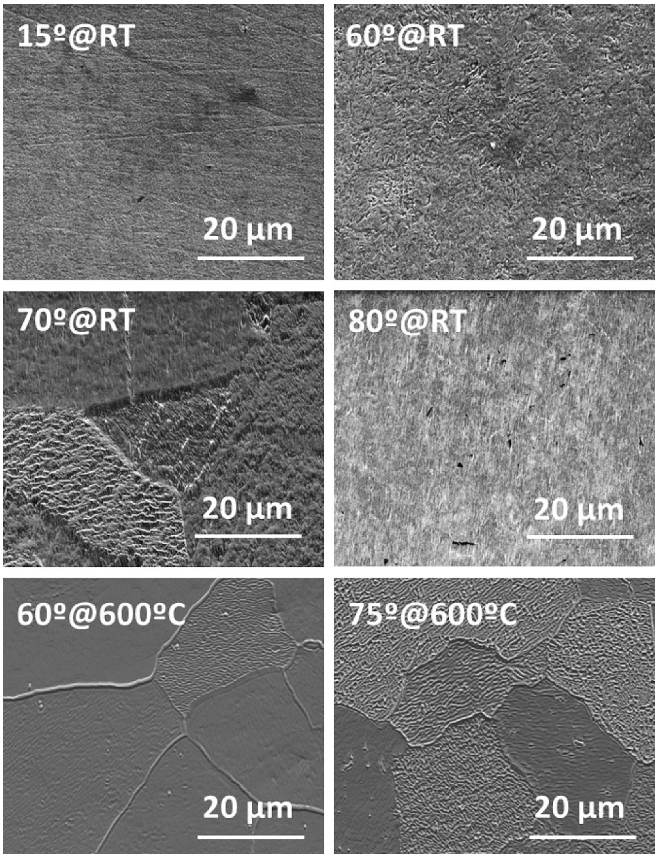

Fig. 4. Low-magnification FE-SEM images of Ti targets irradiated at different α_i values and target temperatures for a dose of 10^{18} ions/cm^2.

mechanisms at elevated temperatures. In other words, within each grain, the crystalline orientation dictates the orientation of the ripples, whose wavelength scales with the increased surface-diffusion distance [19].

Another interesting morphological feature is the formation of facets and pillars for α_i values between 65° and 75°. Again, this behavior is reminiscent of experimentally obtained results for the low-energy irradiation of semiconductors like Si for sufficiently high (but not glancing) incident angles, where facets and "fins" are found, e.g., in [44] and the references therein. In our case, due to the lack of lateral homogeneity in the irradiated polycrystalline targets, both morphologies may coexist with variable characteristic features, making it difficult to assign a definite window for the conditions driving the formation of each morphology. Nevertheless, the FE-SEM images in Fig. 1 suggest that the formation of tip structures is promoted at larger angles. To understand the evolution of such features, we produced a set of samples at $\alpha_i = 75°$ for different ion doses. The results are shown in Fig. 5. Note that there are some discrepancies with respect to the morphologies shown in Fig. 1 since the samples were produced at different temporal stages. Nevertheless, the evolution of the morphology suggests that progressive fragmentation of the terraces occurs with increasing dose (irradiation time), leading to the sculpting of pillars and needles. This process is possibly initiated in the defects within the terraces. Hence, the appearance of facets and pillars in Fig. 1 may be a dynamic process originating from the combined effect of the incidence geometry of the ion beam and corresponding erosion rate.

3.2. Biological assays

A preliminary parameter of interest in evaluating the eventual response of biomolecules over surfaces is the wettability. This is quantified by the relationship between the surface roughness and static contact angle measured after depositing a liquid drop [45,46]. The contact angle strongly depends on the surface morphology. Therefore, wettability tests are necessary to determine the surface contact angles

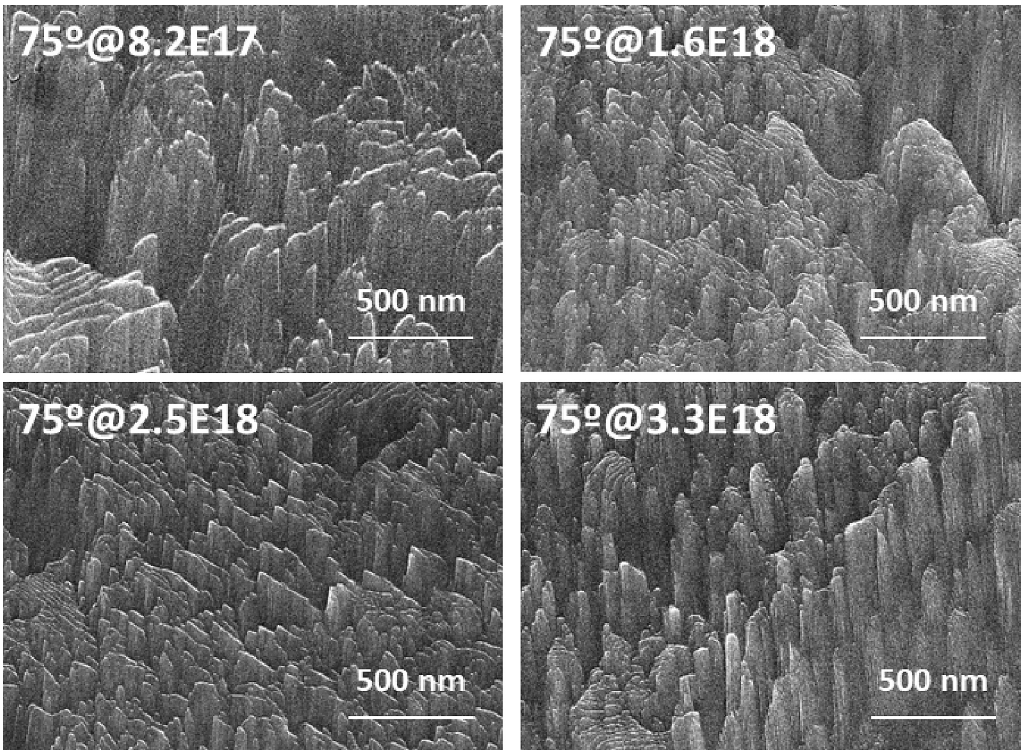

Fig. 5. FE-SEM images of Ti targets irradiated with 1 keV Ar^+ at $\alpha_i = 75°$ for different doses. The projected beam is directed from the top to bottom in the irradiated samples.

for the different morphologies obtained after ion-beam irradiation. The variations in the contact angle for the morphologies shown in Fig. 1 are listed in Table 1. The contact angle for the irradiated surfaces remains within the 90–100° range, with no clear dependence on the incident angle. However, there is a significant change with respect to the non-irradiated targets, since the pristine targets have a contact angle of ~70°. These results indicate that the ion-beam-induced surface morphologies change the wettability of the surface, thereby imparting a higher level of hydrophobicity. As a comparison, Fig. 6 shows the static contact angle measurements on the substrates employed in the bioactivity MTT assays. Likewise, in a recent work of Vandana and collaborators [47], surface effects have been reviewed after noble ion irradiation of single Si (100) crystals. Their work showed a decrease of the surface contact angle as the surface roughness is increased. This result also highlights the significance of the surface energy as influenced by its chemical composition. That is, some of the bombarding ions may remain at the near surface region due to their penetration depth consequently modifying the surface energy. Nonetheless, in low energies irradiations few ions would remain at the near surface region.

The pristine and ion-beam-irradiated surfaces were subjected to MTT assays to determine the proliferation, viability, and cytotoxicity of the treated surfaces [37]. Characteristic morphologies within the diffusive (ripples in fingerprint-like patterns) and erosive (pillar/tip structures) regimes were considered to correspond to irradiation conditions of $\alpha_i = 60°$ and 75°. The results from the MTT assays performed after 72 and 144 h are shown in Fig. 7. The measurement times are relatively high to compensate for possible contact inhibition effects. The results from the (positive) control sample (i.e., cells directly seeded on the multiwell cell culture plate) are also included to verify the effectiveness of cell proliferation. After 72 h, the surface irradiated at $\alpha_i = 60°$ displays an activity that is much higher than in the case of the pristine surface, and similar to that of the control. At this stage, the surface with the tip morphologies produced at $\alpha_i = 75°$ seem to be perform slightly worse than the pristine case. Further evolution of the culture after 144 h reveals that the yields from both irradiated surfaces exceed that of the untreated sample. The activity of the surface irradiated at $\alpha_i = 60°$ appears to be mostly saturated at 72 h, since there is no significant cell proliferation (contrary to the result for the positive control). Nevertheless, the performance is superior to that of the pristine surface, which shows a decrease in the bioactivity with prolonged exposure. In addition, the performance of the sample produced at $\alpha_i = 75°$ appears to improve with time, although the final cell proliferation is still below that reached in the fingerprint-like case. Thus, it is expected that tests at shorter times could provide further insights into the bioactivity of each surface.

In summary, the surface irradiation of Ti targets with low-energy ions enhances the biological response, as determined by comparing the untreated samples to those subjected to ion-beam irradiation. Likewise, the variation in the pattern also seems to influence the overall biocompatibility and temporal response. Nevertheless, further studies are required to describe the general biomedical behavior of the treated substrates under noble ion-beam irradiation and elucidate the influence of the size, shape, and distribution of the topographical features.

4. Conclusions

Ti targets were irradiated with low-energy 1 keV Ar^+ in the range of normal to grazing incidence. The resulting texturization of the Ti surfaces strongly depended on the incident angle, and three types of characteristic morphologies were identified. First, ripples arranged in fingerprint-like patterns were obtained for $\alpha_i \leq 60°$. For $\alpha_i \geq 65°$, the morphology exhibited faceting, with the formation of terraces that were progressively sculpted to form pillar structures pointing toward the ion beam at $\alpha_i \approx 75°$. Finally, shallow ripples parallel to the ion-beam projection were obtained at grazing incidence ($\alpha_i \approx 80°$). This morphological selectivity was attributed to the dominance of diffusive ($\alpha_i \leq 60°$) or erosive ($\alpha_i \geq 65°$) mechanisms as a function of α_i. This interpretation was supported by complementary experiments under axial rotation of the target during irradiation, and by elucidating the morphological evolution at different doses. Finally, the lateral homogeneity of the morphology was discussed in terms of the polycrystalline nature of the targets and the characteristic lateral sizes related to the target microstructure.

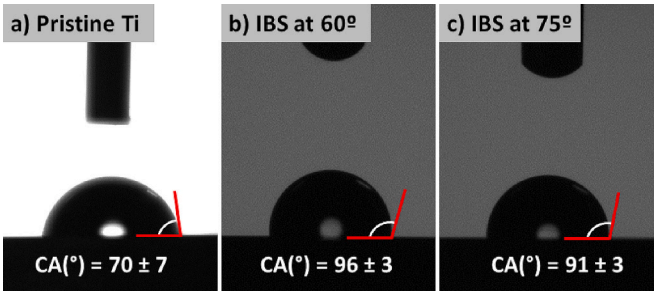

Fig. 6. Static contact angle measurements on polycrystalline titanium substrates. These substrates correspond to those employed on the MTT assays of (a) Pristine surfaces, and ion irradiated surfaces at incidence angles of (b) 60° and at (c) 75°.

Bioactivity MTT assays were performed in samples with selected morphology types. An enhanced bioactivity was obtained for irradiated surfaces compared to the pristine Ti targets, especially under long cell-culture times. These results suggest the possible biomedical applications of irradiated surfaces in dental and orthopedic implants. However, further studies on the bio-chemical interactions of modified surfaces are needed to understand the mechanisms that drive the initial interaction of the surface with the biofluids, as well as the role played by the attainable morphologies on the final performance.

CRediT authorship contribution statement

M.A. Garcia: Conceptualization, Methodology, Investigation, Formal analysis, Visualization, Writing – original draft. **R. Gago:** Supervision, Writing – review & editing, Project administration, Resources, Funding acquisition. **M. Arroyo-Hernández:** Methodology, Investigation, Validation. **E.H. de Laorden:** Investigation. **M. Iglesias:** Methodology, Funding acquisition. **D. Esteban-Mendoza:** Investigation. **R. Cuerno:** Supervision, Writing – review & editing, Funding acquisition. **J. Rickards:** Writing – review & editing, Resources, Funding acquisition.

Declaration of competing interest

The authors declare that they have no known competing financial interests or personal relationships that could have appeared to influence the work reported in this paper.

Table 1
Contact angles (CAs) of samples irradiated with 1 keV Ar^+ at different α values.

Sample	Target	0°	15°	30°	45°	60°	65°	70°	75°	80°
CA (°)	70 ± 7	93 ± 4	97 ± 2	95 ± 2	97 ± 2	96 ± 3	95 ± 4	99 ± 2	91 ± 3	91 ± 3

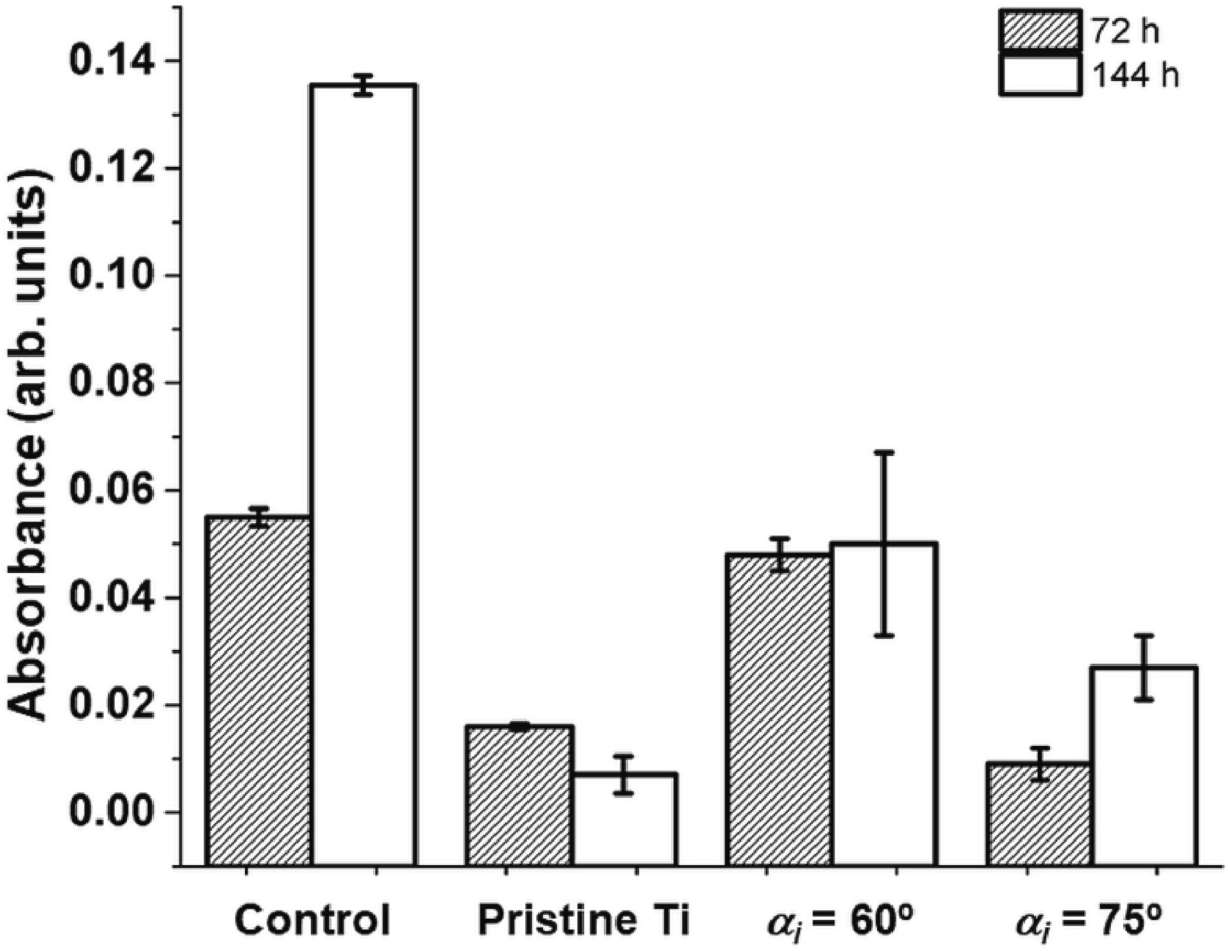

Fig. 7. Absorbance (MTT assay) after 72 h and 144 h of cell culture on bare Ti targets and those irradiated at $\alpha_i = 60°$ and $\alpha_i = 75°$. The results from a multiwell cell-culture plate are used as a positive control for cell proliferation.

Data availability

Data will be made available on request.

Acknowledgments

We thank Prof. L. Vázquez for the fruitful discussions and atomic force microscopy tests, Dr. M. Manso for providing access to conduct the contact angle measurements, and Dr. J. F. Bartolomé for support in polishing the target. We also acknowledge *Instituto de Micro y Nanotecnología* (CSIC) for access to the FE-SEM equipment at the MiNa Laboratory.

Funding

This research was financially supported by Dirección General de Asuntos del Personal Académico (DGAPA) from Universidad Nacional Autónoma de México (UNAM) under grant PAPIIT IN-114120, by Ministerio de Ciencia, Innovación y Universidades (Spain), Agencia Estatal de Investigación (AEI, Spain), and Fondo Europeo de Desarrollo Regional (FEDER, EU) through grants PGC2018-094763-B-I00, PID2021-123969NB-I00, and by Comunidad de Madrid (Spain) under the Multiannual Agreement with UC3M for Excellence of University Professors (EPUC3M23), in the context of the "V Plan Regional de Investigación Científica e Innovación Tecnológica" (PRICIT). Additional funding was obtained from Consejo Nacional de Ciencia y Tecnología (CONACyT, Mexico) under "Estancias Posdoctorales en el Extranjero Vinculadas a la Consolidación de Grupos de Investigación y Fortalecimiento del Posgrado Nacional" with scholarship numbers 711146, and 740556.

References

[1] T. Hanawa, Overview of metals and applications, in: M. Niinomi (Ed.), Metals for Biomedical Applications, Second Edition, Woodhead Publishing – Elsevier Ltd, Duxford, 2019, pp. 3–29.
[2] B.D. Ratner, A.S. Hoffman, F.J. Schoen, J.E. Lemons, Biomaterials Science, an Introduction to Materials in Medicine, Third ed., Elsevier Inc., Oxford, 2013.
[3] J. Breme, E. Eisenbarth, V. Biehl, Titanium and its alloy for medical applications, in: C. Leyens, M. Peters (Eds.), Titanium and Titanium Alloys – Fundamentals and Applications, Wiley-VCH Verlag GmbH & Co. KGaA, Weiheim, 2003, pp. 423–451.
[4] K. Grandfield, Bone, implants, and their interfaces, Phys. Today 68 (2015) 40–45, https://doi.org/10.1063/PT.3.2748.
[5] Q. Chen, G.A. Thouas, Metallic implant biomaterials, Mater. Sci. Eng. R 87 (2015) 1–57, https://doi.org/10.1016/j.mser.2014.10.001.
[6] M. Kaur, K. Singh, Review on titanium and titanium based alloys as biomaterials for orthopaedic applications, Mater. Sci. Eng. C 102 (2019) 844–862, https://doi.org/10.1016/j.msec.2019.04.064.
[7] S. Maghsoudi, N. Rabiee, S. Ahmadi, M. Rabiee, M. Bagherzadeh, M. Karimi, An overview of microfluid devices, in: M.R. Hamblin, M. Karimi (Eds.), Biomedical Applications of Microfluidic Devices, Elsevier Inc., London, 2021, pp. 1–22.
[8] S.C. Gad, S. Gad-McDonald, Chapter 16 – special case devices, and chapter 17 – combination products, in: Biomaterials, Medical Devices, and Combination Products – Biocompatibility Testing, and Safety Assessment, Taylor & Francis Group LLC, Boca Raton, 2016, pp. 371–398.
[9] B. Ziaie, A. Baldi, M.Z. Atashbar, Introduction to micro/nanofabrication, in: B. Bhushan (Ed.), Springer Handbook of Nanotechnology, Springer Science+ Business Media Inc, Berlin, 2007, pp. 197–237.
[10] M. Nastasi, J.W. Mayer, Ion Implantation and Synthesis of Materials, Springer-Verlag, Berlin, 2006.
[11] J. Muñoz-García, L. Vázquez, R. Cuerno, J.A. Sanchez-García, M. Castro, R. Gago, Self-organized surface nanopattering by ion beam sputtering, in: Z.M. Wang (Ed.),

Toward Functional Nanomaterials, Lecture Notes in Nanoscale Science and Technology, 5, Springer-Science+Business Media,LCC, 2009, pp. 323–398.
[12] C. Moseke, U. Gbureck, Surface treatment, in: M. Niinomi (Ed.), Metals for Biomedical Applications, Second Edition, Woodhead Publishing – Elsevier Ltd., Duxford, 2019, pp. 355–367.
[13] L. Hao, J. Lawrence, Laser Surface Treatment of Bio-Implant Materials, John Wiley & Sons Ltd, West Sussex, 2005.
[14] M. Kulkarni, A. Mazare, E. Gongadze, Š. Perutkova, V. Kralj-Iglič, I. Milošev, P. Schmuki, A. Iglič, M. Mozetič, Titanium nanostructures for biomedical applications, Nanotechnology 26 (2015), 062002, https://doi.org/10.1088/0957-4484/26/6/062002.
[15] D.M. Brunette, P. Tengvall, M. Textor, P. Thomsen, Titanium in Medicine – Materials Science, Surface Science, Engineering, Biological Response and Medical Applications, Springer-Verlag, Berlin, 2001.
[16] Y. Ikada, Tissue Engineering Fundamentals and Applications, Elsevier Ltd., Amsterdam, 2006.
[17] R. Cuerno, J.-S. Kim, A perspective on nanoscale pattern formation at surfaces by ion-beam irradiation, J. Appl. Phys. 128 (2020), 180902, https://doi.org/10.1063/5.0021308.
[18] T. Aste, U. Valbusa, Ripples and ripples: from sandy deserts to ion-sputtered surfaces, New J. Phys. 7 (2005) 122, https://doi.org/10.1088/1367-2630/7/1/122.
[19] U. Valbusa, C. Boragno, F. Buatier de Mongeot, Nanostructuring surfaces by ion sputtering, J. Phys. Condens. Matter 14 (2002) 8153–8175, https://doi.org/10.1088/0953-8984/14/35/301.
[20] J. Muñoz-García, L. Vázquez, M. Castro, R. Gago, A. Redondo-Cubero, A. Moreno-Barrado, R. Cuerno, Self-organized nanopattering of silicon surfaces by ion beam sputtering, Mater. Sci. Eng. R 86 (2014) 1–44, https://doi.org/10.1016/j.mser.2014.09.001.
[21] F. Buatier de Mongeot, U. Valbusa, Applications of metal surfaces nanostructured by ion beam sputtering, J. Phys. Condens. Matter 21 (2009), 224022, https://doi.org/10.1088/0953-8984/21/22/224022.
[22] W.L. Chan, E. Chason, Making waves: kinetic processes controlling surface evolution during low energy ion sputtering, J. Appl. Phys. 101 (2007), 121301, https://doi.org/10.1063/1.2749198.
[23] M.C. Giordano, F. di Sacco, M. Barelli, G. Portale, F. Buatier de Mongeot, Self-organized tailoring of faceted glass nanowrinkles for organic nanoelectronics, ACS Appl. Nano Mater. 4 (2021) 1940–1950, https://doi.org/10.1021/acsanm.0c03290.
[24] M.C. Giordano, F. Buatier de Mongeot, Anisotropic nanoscale wrinkling in solid-state substrates, Adv. Mater. 30 (2018), 1801840, https://doi.org/10.1002/adma.201801840.
[25] A. Keller, S. Facsko, W. Möller, The morphology of amorphous SiO2 surfaces during low energy ion sputtering, J. Phys. Condens. Matter 21 (2009), 495305, https://doi.org/10.1088/0953-8984/21/49/495305.
[26] E. Lee, J. Seo, J. Muñoz-García, M. Castro, R. Cuerno, J.-S. Kim, Nanopatterning of rotating highly oriented pyrolytic graphite (0001) surfaces by ion beam irradiation: experiments and modeling, Phys. Rev. B 105 (2022), 085413, https://doi.org/10.1103/PhysRevB.105.085413.
[27] T. Škereň, K. Temst, W. Vandervorst, A. Vantomme, Ion-induced roughening and ripple formation on polycrystalline metallic films, New J. Phys. 15 (2013), 093047, https://doi.org/10.1088/1367-2630/15/9/093047.
[28] Y. Yang, A. Keller, Ion beam nanopatterning of biomaterial surfaces, Appl. Sci. 11 (2021) 6575, https://doi.org/10.3390/app11146575.
[29] M.-K. Lee, H. Lee, H.-E. Kim, E.-J. Lee, T.-S. Jang, H.-D. Jung, Nano-topographical control of Ti-Nb-Zr alloy surfaces for enhanced osteoblastic response, Nanomaterials 11 (2020) 1507, https://doi.org/10.3390/nano11061507.
[30] N.A. Riedel, S.L. Bechara, K.C. Popat, J.D. Williams, Ion etching for sharp tip features on titanium and the response of cells to these surfaces, Mater.Lett. 81 (2012) 158–161, https://doi.org/10.1016/j.matlet.2012.04.147.
[31] N.A. Riedel, J.D. Williams, K.C. Popat, Ion beam etching titanium for enhanced osteoblast response, J. Mater. Sci. 46 (2011) 6087–6095, https://doi.org/10.1007/s10853-011-5571-z.
[32] J. Bauer, F. Frost, Orientation-dependent nanostructuring of titanium surfaces by low-energy ion beam erosion, Surf. Interface Anal. 52 (2020) 1071–1076, https://doi.org/10.1002/sia.6764.
[33] M.A. Garcia, R. Gago, D. Esteban-Mendoza, R. Cuerno, J. Rickards, Morphological impact of low-energy Xe+ irradiation on polycrystalline titanium targets, J. Phys. Conf. Ser. 1593 (2020), 012041, https://doi.org/10.1088/1742-6596/1593/1/012041.
[34] M.A. Garcia, J. Rickards, R. Cuerno, R. Trejo-Luna, J. Cañetas-Ortega, L.R. de la Vega, L. Rodríguez-Fernández, Surface morphologies of Ti and Ti-Al-V bombarded by 1.0-MeV Au+ ions, Phys. Rev. Appl. 8 (2017), 064027, https://doi.org/10.1103/PhysRevApplied.8.064027.
[35] V.B. Shenoy, W.L. Chan, E. Chason, Compositionally modulated ripples induced by sputtering of alloy surfaces, Phys. Rev. Lett. 98 (2007), 256101, https://doi.org/10.1103/PhysRevLett.98.256101.
[36] Goodfellow Corp. is based in Pennsylvania, USA.
[37] S.C. Gad, S. Gad-McDonald, Chapter 6 – cytotoxicity testing, in: Biomaterials, Medical Devices, and Combination Products – Biocompatibility Testing, and Safety Assessment, Taylor & Francis Group LLC, Boca Raton, 2016, pp. 111–121.
[38] G. Carter, The effects of surface ripples on sputtering erosion rates and secondary ion emission yields, J. Appl. Phys. 85 (1999) 455–459, https://doi.org/10.1063/1.369408.
[39] A. Toma, B. Šetina Batič, D. Chiappe, C. Boragno, U. Valbusa, M. Godec, M. Jenko, F. Buatier de Mongeot, Patterning polycrystalline thin films by defocused ion beam: the influence of initial morphology on the evolution of self-organized nanostructures, J. Appl. Phys. 104 (2008), 104313, https://doi.org/10.1063/1.3021100.
[40] A. Toma, D. Chiappe, B. Šetina Batič, M. Godec, M. Jenko, F. Buatier de Mongeot, Erosive versus shadowing instabilities in the self-organized ion patterning of polycrystalline metal films, Phys. Rev. B 78 (2008), 153406, https://doi.org/10.1103/PhysRevB.78.153406.
[41] J.F. Ziegler, M.D. Ziegler, J.P. Biersack, SRIM – the stopping and range of ions in matter (2010), Nucl. Instrum. Methods Phys. Res. Sect. B 268 (2010) 1818–1823, https://doi.org/10.1016/j.nimb.2010.02.091.
[42] M. Engler, S. Macko, F. Frost, T. Michely, Evolution of ion beam induced patterns on Si(001), Phys. Rev. B 89 (2014), 245412, https://doi.org/10.1103/PhysRevB.89.245412.
[43] D. Nečas, P. Klapetek, Gwyddion: an open-source software for SPM data analysis, Cent. Eur. J. Phys. 10 (2012) 181–188, https://doi.org/10.2478/s11534-011-0096-2.
[44] J. Seo, D.A. Pearson, R.M. Bradley, J.-S. Kim, Nanoscale pattern formation on silicon surfaces bombarded with a krypton ion beam: experiments and simulations, J. Phys. Condens. Matter 34 (2022), 265001, https://doi.org/10.1088/1361-648X/ac64df.
[45] I. Mutreja, Z. Ye, C. Aparicio, Chapter 19 – cell responses to titanium and titanium alloys, in: M. Mozafari (Ed.), Handbook of Biomaterials Biocompatibility, Woodhead Publishing – Elsevier Ltd., Duxford, 2020, pp. 423–452.
[46] D. Bonn, J. Eggers, J. Indekeu, J. Meunier, E. Rolley, Wetting and spreading, Rev. Mod. Phys. 81 (2009) 739–805, https://doi.org/10.1103/RevModPhys.81.739.
[47] Vandana, T. Kumar, S. Ojha, S. Kumar, Energy-dependent surface nanopatterning of Si (100) for different projectiles: a tunable anisotropic wettability of ripple surface, Appl. Nanosci. (2021), https://doi.org/10.1007/s13204-021-01975-5.